Photophysics of uracil: an explicit time-dependent generating function-based method combining both nonadiabatic and spin-orbit coupling effects†

Pijush Karak,[a‡] Torsha Moitra,[b‡] Kenneth Ruud,[*b,c] and Swapan Chakrabarti[*a]

We present a composite framework for calculating the rate of non-radiative deactivation processes, namely internal conversion (IC) and intersystem crossing (ISC), on an equal footing by explicitly computing the non-adiabatic coupling (NAC) and spin-orbit coupling (SOC) constants, respectively. The stationary-state approach uses a time-dependent generating function based on Fermi´s Golden rule. We validate the applicability of the framework by computing the rate of IC for azulene, obtaining comparable rates to experimental and previous theoretical results. Next, we investigate the photophysics associated with the complex photodynamics of uracil molecule. Interestingly, our simulated rates corroborates experimental observations. Detailed analysis using Duschinsky rotation matrices, displacement vectors and NAC matrix elements are presented to interpret the findings alongside testing the suitability of the approach for such molecular systems. The suitability of the Fermi´s Golden rule based method is explained qualitatively in terms of single-mode potential energy surfaces.

1 Introduction

The photophysics following light-matter interactions that lead to a population of the excited state of a molecule, constitutes a fundamental process in nature. The excited molecule relaxes using multiple channels, often highly entangled. As a consequence, understanding the photophysical deactivation pathway enabling the self-protection mechanism of DNA and RNA nucleobases forms one of the most intriguing questions in science.[1–34] One of the most common photophysical decay processes is the spin-conserved internal conversion (IC) between a pair of same-spin electronic states. Alongside, there also occurs non-raditative spin-forbidden transitions, called intersystem crossings (ISC). The time-scale of deactivation usually ranges from a few femtoseconds to pico-seconds, thereby involving nuclear motion induced evolution of the molecular geometry and the electronic properties simultaneously. The theoretical treatment of the time-dependent nonadiabatic processes for molecular systems is a challenging task, due to the need to describe excited states as well as time propagate molecular properties. Several strategies have been developed, implemented and used over the decades to study various photo-dynamic processes. The most general and accurate method would be a full quantum mechanical propagation of the wave packet. However, this can prove to be computationally too expensive for chemically relevant systems, calling for more approximate methods.

Semi-classical trajectory surface hopping (TSH) has gained popularity. In TSH, the non-adiabatic states of systems are propagated in time. It relies on the hypothesis that time evolution of the wave packet can be represented by an ensemble of independent semi-classical trajectories stochastically distributed among different branching potential energy surfaces. The method has been most commonly used due to its intuitive conceptual background and the availability of efficient implementations in quantum chemistry software, among other reasons. However, the method is not infallible. For instance, the coherence between states can be inconsistent because of the independent trajectory approach. Quite often, the TSH technique is used to study the dynamics near conical intersections relevant for IC. However, this is not the only plausible mechanism for IC as shown by Farfan and Turner,[35] where they show that inaccessible conical intersections can also induce nonadiabatic population transfer as efficiently as directly achieved via conical intersection. More recently, Mukherjee and Barbatti have proposed that ultrafast IC can occur between electronic states without energetically accessible conical intersections, when the molecule remains in a region of relatively weak non-adiabatic coupling, increasing the chances of less probable transitions.[36] They show that small gap potential energy surfaces are suitable for such a mechanism of ultrafast IC. Besides, Santoro and co-workers have shown recently, using a linear-vibronic coupling framework, that energetically accessible conical intersections are not a necessary condition for describing ultrafast decay processes in pyrene[37] and uracil.[33] Furthermore, generalized ab initio multiple spawning based approaches can be employed for computing nonadiabatic dynamics involving both the IC and ISC transitions in molecules of moderate size.[38]

Another school of methodologies[39–45] exists based on first-order perturbation theory, known as Fermi´s Golden rule (FGR),

[a] Department of Chemistry, University of Calcutta, 92 A.P.C Road, Kolkata - 700009, West Bengal, India.
[b] Hylleraas Centre for Quantum Molecular Sciences, Department of Chemistry, University of Tromsø – The Arctic University of Norway, 9037 Tromsø, Norway.
[c] Norwegian Defence Research Establishment, P.O.Box 25, 2027 Kjeller, Norway.
E-mail: swcchem@caluniv.ac.in, kenneth.ruud@uit.no
† Electronic Supplementary Information (ESI) available: [details of any supplementary information available should be included here].
‡ These authors contributed equally to this work.

which are often computationally more practical for complex molecular systems. This method is applicable within the Franck-Condon region, and employs Duschinsky rotation effects mixing different vibrational modes of different electronic states. In the Duschinsky rotation, both electronic states (usually ground and excited state) are described by different harmonic parabolas, where the normal modes of one electronic state can be expressed as a linear combination of all the normal modes of another parabola. The use of a canonical probability function in the expression for the rate constants ensures that the effect of temperature on the non-radiative rate processes is included. Although FGR based methods successfully include Duschinsky mixing and thermal effects, its use is limited to systems having large electronic energy gap and also to systems where non-radiative quantum processes occur far away from equilibrium. Nevertheless, FGR-based methods lack the treatment of out-of-equilibrium processes and coherence phenomenon. Despite the fundamental limitations of FGR approaches to describe quantum effects like coherence, detailed comparative studies between quantum dynamics and FGR for moderately-sized molecules show qualitative agreement in the computed rate constants, as reported by Liu *et al.*.[46].

In this article, we present an open-source implementation for computing the rate of IC, within the Fermi´s Golden rule using time-dependent correlation functions. This forms the final missing piece in our tool-kit for studying photophysical processes. Previously, we have presented computational setups for simulating the rate of ISC using cumulant expansions[47] and correlation functions.[48,49] More recently, we have also formulated a methodology for calculating the rate of reverse ISC incorporating spin-vibronic interactions.[50] We believe that all these open-source codes together will be a valuable computational tool for a wide audience in the field of ultrafast dynamics.

We begin by briefly laying the theoretical foundation for calculating the rates of IC and ISC in Section 2.1 and 2.2. A final compact expression for calculating the rates of IC and ISC, with all essential components driving the processes, are identified here. The details of the quantum-chemical computational setup is given in Section 3. We first validate our implementation by investigating the rate of IC for the azulene molecule in Section 4.1. Then, we study the highly complex and debated decay mechanism of the nucleobase uracil. Our findings are presented in Section 4.2. The choice of the system is primarily governed by the plethora of literature (both experimental and theoretical) results available for comparison. The major findings and prospects of the method is summarized in Section 5.

2 Theoretical background

2.1 Rate of internal conversion (IC)

To formulate the rate constant of IC, one has to go beyond the Franck-Condon approximation where first-order perturbation theory is applied to the non-Born–Oppenheimer Hamiltonian. We follow the methodology proposed by Peng *et al.* [42] to compute the rate of IC including Duschinsky rotation effects. The expression for the IC rate constant within the framework of Fermi's golden rule is given by,

$$\mathrm{k_{IC}} = \frac{2\pi}{\hbar Z}\sum_{i,j} e^{-\beta E_{v_{ai}}} |\hat{H}^{\mathrm{nBO}}|^2 \delta(\Delta E_{ab} + E_{v_{ai}} - E_{v_{bj}}), \tag{1}$$

where the initial and final vibronic states are defined by v_{ai} and v_{bj} with a and b representing the electronic states and the vibrational levels are denoted by i and j, respectively. ΔE_{ab} is the energy gap between the ath and bth electronic states. $\hat{H}^{\mathrm{nBO}}$ is the non-Born–Oppenheimer operator coupling the two different electronic states a and b via the nuclear momentum operator. Under the Condon approximation, the electronic and vibrational contributions are decoupled, leading to an expression for $\hat{H}^{\mathrm{nBO}}$ as,

$$\hat{H}^{\mathrm{nBO}} = -\hbar^2 \sum_m \langle \psi_{a_{\mathrm{electronic}}} | \frac{\partial}{\partial \mathbf{Q}_m} | \psi_{b_{\mathrm{electronic}}} \rangle \langle \psi_{v_i} | \frac{\partial}{\partial \mathbf{Q}_m} | \psi_{v_j} \rangle \ . \tag{2}$$

In the above equation, $\mathbf{Q_m}$ denotes the normal coordinate of the $m-$th normal mode. Here, Z is the partition function having the mathematical form $\sum_i e^{-\beta E_{v_{ai}}}$, where $\beta = \frac{1}{kT}$ with k and T representing the Boltzman constant and temperature, respectively. The electronic and vibrational states in this equation are defined as $\psi_{a/b_{electronic}}$ and $\psi_{vi/j}$, respectively. Substituting this equation into the Eq. (1), the rate constant considering contributions from all pairs (m,m') of vibrational normal modes becomes,[42,51,52]

$$\mathrm{k_{IC}} = \frac{2\pi}{\hbar Z}\sum_{m,m'} T_{m,m'} \sum_{i,j} e^{-\beta E_{v_{ai}}} P_{m,m'} \delta(\Delta E_{ab} + E_{v_{ai}} - E_{v_{bj}}) \ ; \tag{3}$$

where,

$$T_{m,m'} = -\hbar^2 \langle \psi_{a_{\mathrm{electronic}}} | \frac{\partial}{\partial \mathbf{Q}_m} | \psi_{b_{\mathrm{electronic}}} \rangle \langle \psi_{b_{\mathrm{electronic}}} | \frac{\partial}{\partial \mathbf{Q}_{m'}} | \psi_{a_{\mathrm{electronic}}} \rangle \tag{4}$$

$$P_{m,m'} = -\hbar^2 \langle \psi_{v_i} | \frac{\partial}{\partial \mathbf{Q}_m} | \psi_{v_j} \rangle \langle \psi_{v_j} | \frac{\partial}{\partial \mathbf{Q}_{m'}} | \psi_{v_i} \rangle \ . \tag{5}$$

The term $T_{m,m'}$ is known as the NAC vector between the two electronic states a and b.

Fourier transforming the integral in Eq. (3) into the time domain and using Feynman's path integral formulation for trace calculation over the final electronic states, followed by multidimensional Gaussian integrations, the final rate expression incorporating both the Franck-Condon (FC) and Herzberg-Teller (HT) terms is given by,[42,51,53]

$$\mathrm{k_{IC}} = \frac{1}{\hbar^2 Z}\sum_{m,m'} T_{m,m'} \int_{-\infty}^{\infty} G_{\mathrm{IC}}^{\mathrm{FC+HT}}(t,t';m,m') e^{\frac{i}{\hbar}\Delta E_{\mathrm{ab}} t} dt. \tag{6}$$

where the correlation functions comprising the FC and HT terms are given by Eq. (7) and (8), respectively.

$$G_{\mathrm{IC}}^{\mathrm{FC}}(t,t') = \sqrt{\frac{\det(\mathbf{S}_i)\det(\mathbf{S}_f)}{\det(\mathbf{W})}} exp(-\frac{i}{2\hbar}\mathbf{V}^{\mathrm{T}}\mathbf{W}^{-1}\mathbf{V} + \frac{i}{\hbar}\mathbf{D}^{\mathrm{T}}\mathbf{U}\mathbf{D}), \tag{7}$$

$$G_{\mathrm{IC}}^{\mathrm{HT}}(t,t';m,m') = i\hbar \mathrm{Tr}(\mathbf{X}\mathbf{W}^{-1}) + (\mathbf{W}^{-1}\mathbf{V})^{\mathrm{T}}\mathbf{X}(\mathbf{W}^{-1}\mathbf{V}) - \mathbf{Y}^{\mathrm{T}}\mathbf{W}^{-1}\mathbf{V} \tag{8}$$

Therefore, the total correlation function can be defined as,

$$G_{\mathrm{IC}}^{\mathrm{FC+HT}}(t,t';m,m') = G_{\mathrm{IC}}^{\mathrm{FC}}(t,t')G_{\mathrm{IC}}^{\mathrm{HT}}(t,t';m,m') \ . \tag{9}$$

In Eq. (9) $t' = -i\beta - t\hbar^{-1}$. The other terms in Eqs. (7) and (8) are,

$$\mathbf{S}_f = \frac{\omega_f}{sin(\omega_f t\hbar)}; \ \mathbf{B}_f = \frac{\omega_f}{tan(\omega_f t\hbar)};$$

$$\mathbf{S}_i = \frac{\omega_i}{sin(\omega_i t'\hbar)}; \ \mathbf{B}_i = \frac{\omega_i}{tan(\omega_i t'\hbar)};$$

$$\mathbf{W} = \begin{bmatrix} \mathbf{B}_f + \mathbf{J}^{\mathrm{T}}\mathbf{B}_i\mathbf{J} & -(\mathbf{S}_f + \mathbf{J}^{\mathrm{T}}\mathbf{S}_i\mathbf{J}) \\ -(\mathbf{S}_f + \mathbf{J}^{\mathrm{T}}\mathbf{S}_i\mathbf{J}) & \mathbf{B}_f + \mathbf{J}^{\mathrm{T}}\mathbf{B}_i\mathbf{J} \end{bmatrix}; \ \mathbf{U} = (\mathbf{B}_i - \mathbf{S}_i);$$

$$\mathbf{V} = \begin{bmatrix} \mathbf{J}^{\mathrm{T}}\mathbf{U}\mathbf{D} \\ \mathbf{J}^{\mathrm{T}}\mathbf{U}\mathbf{D} \end{bmatrix};$$

$$\mathbf{X} = \begin{bmatrix} \mathbf{X}_{11}(m,m') & \mathbf{X}_{12}(m,m') \\ \mathbf{X}_{21}(m,m') & \mathbf{X}_{22}(m,m') \end{bmatrix}; \ \mathbf{Y} = \begin{bmatrix} \mathbf{Y}_1(m,m') \\ \mathbf{Y}_2(m,m') \end{bmatrix};$$

$$\mathbf{X}(m,m') = \begin{bmatrix} 0 & 0 \\ . & . \\ . & . \\ . & . \\ 0 & 0 \\ -(\mathbf{B}_f)_{m,m}(\mathbf{J}^{\mathrm{T}}\mathbf{S}_i\mathbf{J})_{m'} & (\mathbf{B}_f)_{m,m}(\mathbf{J}^{\mathrm{T}}\mathbf{B}_i\mathbf{J})_{m'} \\ 0 & 0 \\ . & . \\ . & . \\ . & . \\ 0 & 0 \\ 0 & 0 \\ . & . \\ . & . \\ . & . \\ 0 & 0 \\ (\mathbf{S}_f)_{m,m}(\mathbf{J}^{\mathrm{T}}\mathbf{S}_i\mathbf{J})_{m'} & -(\mathbf{S}_f)_{m,m}(\mathbf{J}^{\mathrm{T}}\mathbf{B}_i\mathbf{J})_{m'} \\ 0 & 0 \\ . & . \\ . & . \\ . & . \\ 0 & 0 \end{bmatrix};$$

$$\mathbf{Y}(m,m') = \begin{bmatrix} 0 \\ . \\ . \\ . \\ 0 \\ (\mathbf{B}_f)_{m,m}(\mathbf{J}^{\mathrm{T}}\mathbf{U}\mathbf{D})_{m'} \\ 0 \\ . \\ . \\ . \\ 0 \\ 0 \\ . \\ . \\ . \\ 0 \\ -(\mathbf{S}_f)_{m,m}(\mathbf{J}^{\mathrm{T}}\mathbf{U}\mathbf{D})_{m'} \\ 0 \\ . \\ . \\ . \\ 0 \end{bmatrix}. \tag{10}$$

In the above expressions, i and f indicates the initial and final states and $\omega, \mathbf{J}$ and $\mathbf{D}$ are the frequency, Duschinsky rotation matrix and displacement vectors, respectively. The normal coordinates of two electronic states are connected through the relation $\mathbf{Q}_f = \mathbf{J}\mathbf{Q}_i + \mathbf{D}$. **W, X** and **V, Y** are $2N \times 2N$ and $2N \times 1$ matrix and vector and diagonal matrices are defined by **S** and **B**, respectively. **U** is the $N \times 1$ column vector.

2.2 Rate of intersystem crossing (ISC)

Within the Franck–Condon approximation, the rate of ISC can be obtained applying first-order perturbation theory with the spin-orbit coupling operator as a perturbation and including only the direct term[48,54]

$$\mathrm{k_{ISC}} = \frac{1}{Z}|\langle\psi_S|\hat{H}_{\mathrm{SO}}|\psi_T\rangle|^2_{q_0} \times \int_{-\infty}^{\infty} G_{\mathrm{ISC}}(t)e^{-it\Delta E_{\mathrm{ST}}}dt, \tag{11}$$

where the expression for the time-dependent generating function is defined as,

$$G_{\mathrm{ISC}}(t) = \sqrt{\frac{\det(\mathbf{S}_S^{-1}\mathbf{S}_T^{-1}\mathbf{\Omega}_S\mathbf{\Omega}_T)}{\det(\mathbf{J}^\dagger\mathbf{\Omega}_T\mathbf{B}_T\mathbf{J} + \mathbf{\Omega}_S\mathbf{B}_S)\det(\mathbf{J}^\dagger\mathbf{\Omega}_T\mathbf{B}_T^{-1}\mathbf{J} + \mathbf{\Omega}_S\mathbf{B}_S^{-1})}}$$

$$\times e^{\mathbf{D}^\dagger(\mathbf{\Omega}_T\mathbf{B}_T\mathbf{J}(\mathbf{J}^\dagger\mathbf{\Omega}_T\mathbf{B}_T\mathbf{J}+\mathbf{\Omega}_S\mathbf{B}_S)^{-1}\mathbf{J}^\dagger\mathbf{\Omega}_T\mathbf{B}_T - \mathbf{\Omega}_T\mathbf{B}_T)\mathbf{D}} \tag{12}$$

with $(\mathbf{S}_S)_{ii} = \sinh((\beta - it)(\omega_S)_i)$, $(\mathbf{S}_T)_{ii} = \sinh(i(\omega_T)_i t)$, $)(\mathbf{B}_T)_{ii} = \tanh(\frac{i(\omega_T)_i t}{2})$, $(\mathbf{B}_S)_{ii} = \tanh\left(\frac{(\beta-it)(\omega_S)_i}{2}\right)$ and $(\mathbf{\Omega}_T)_{ii} = (\omega_T)_i$, $(\mathbf{\Omega}_S)_{ii} = (\omega_S)_i$. The i-th normal mode frequency of the singlet and triplet states is represented as $(\omega_S)_i$ and $(\omega_T)_i$ and ΔE_{ST} is the energy

gap between these two states. The spin-orbit coupling operator between the singlet and triplet states and the coordinates of the initial-state equilibrium geometry in the above equation are designated as $\hat{H}_{\rm SO}$ and $\mathbf{q}_0$, respectively. We compute $k_{\rm ISC}$ employing a simplified form of Eq. (11), as derived in Ref. 48

$$k_{\rm ISC} = \frac{2}{Z}|\langle\psi_S|\hat{H}_{\rm SO}|\psi_T\rangle|^2 \int_0^\infty \sqrt{\sqrt{(U^2+V^2)}e^{K_1}}\cos(\frac{\theta}{2}+K_2)dt \tag{13}$$

The notation and the terms are used consistently with Ref. 48.

3 Computational details

We benchmark our new open-source implementation for calculating the rate of IC for the azulene molecule and then apply the composite framework (involving both IC and ISC rate calculation) to understand the decay mechanism of uracil using the Fermi´s Golden rule approach.

We optimize the ground state (S_0), singlet excited states (S_1 for azulene and S_1,S_2 and S_3 for uracil) and triplet excited states (T_1,T_2 and T_3 for uracil) geometries at B3LYP/6-311G(d,p) level of theory as implemented in Gaussian16.[55] Time-dependent density functional theory has been used for optimizing the excited-state geometries. Subsequently, the same level of theory has been used to compute the normal mode frequencies. The ground- and excited-state geometries and frequencies are reported in the supplementary information (SI). The ground-state optimized geometry of uracil is depicted in Fig. 1. We perform single-point energy calculations to estimate the energy gap between electronic states at the multi-state second-order multi-configurational perturbation theory (MS-CASPT2)[56] level with an active space constituted by 10 electrons in 10 orbitals for azulene[57] and 14 electrons in 10 orbitals for uracil in combination with the cc-pVDZ[58] basis set. The state averaging is done over the lowest 5 singlet or triplet states as implemented in BAGEL . We generate the PES corresponding to a particular mode at the different electronic state at the same level of theory using the BAGEL software.[59–62] In order to generate the PES, a displacement was applied along the direction of the displacement vector of the normal mode. At the same level of theory, we compute the non-adiabatic coupling matrix elements (NACMEs) between various electronic states under study

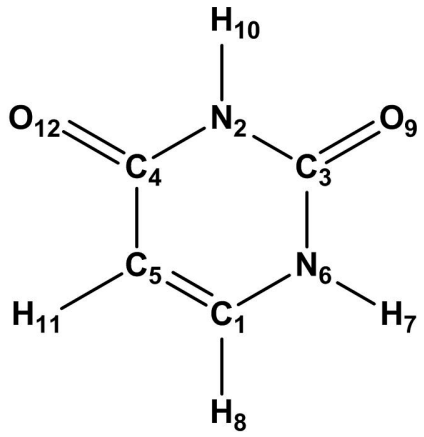

Fig. 1 Ground state optimized structure of uracil.

(namely, S_1-S_0 for azulene and S_3-S_2, S_2-S_1 and T_2-T_1) for uracil. NACMEs are calculated starting from the higher excited state of importance (S_1 for azulene and S_2 for uracil)

We transform the computed non mass-weighted cartesian NAC vectors to the normal mode coordinates with the help of the eigenvector matrix obtained by diagonalizing the mass–weighted Cartesian Hessian as,

$$\langle\psi_{a_{\rm electronic}}|\frac{\partial}{\partial\mathbf{Q}_m}|\psi_{b_{\rm electronic}}\rangle = \sum_k\sum_l L^{\rm T}_{kl}\langle\psi_{a_{\rm electronic}}|\frac{\partial}{\partial\mathbf{q}_{kl}}|\psi_{b_{\rm electronic}}\rangle\frac{1}{\sqrt{M_k}} \tag{14}$$

$$\text{where, } l \in \{x,y,z\} \ ,$$

for the calculation of $k_{\rm IC}$ using Eq. (6). In Eq. 14, the transpose of the eigenvector matrix of the mass–weighted Hessian and the mass of the k-th nucleus are denoted as $L^{\rm T}_{kl}$ and M_k, respectively. $\mathbf{q}$ represents the Cartesian coordinate. Further, the nonadiabatic coupling matrix element (NACME) are expressed as

$$\langle\psi_{a_{\rm electronic}}|\frac{\partial}{\partial\mathbf{Q}_m}|\psi_{b_{\rm electronic}}\rangle = \frac{\langle\psi_{a_{\rm electronic}}|\frac{\partial\hat{V}}{\partial\mathbf{Q}_m}|\psi_{b_{\rm electronic}}\rangle}{E_{a_{\rm electronic}} - E_{b_{\rm electronic}}}, \tag{15}$$

where a, b, E, Q_m and V denotes the electronic states, energy, coordinate of the normal mode and electron-nucleus attraction operator, respectively.

The spin-orbit coupling matrix element (SOCME) between the singlet-triplet states of uracil are computed using def2-TZVP basis at the CASSCF(14e,10o) level of theory as implemented in ORCA 5.0.2. software.[63,64] The optimized S_2 geometry is used for SOCME calculations.

Another ingredient for the calculations of $k_{\rm IC}$ and $k_{\rm ISC}$ is the Duschinsky rotation matrix (**J**) and the displacement vectors (**D**) between two electronic states. We obtain these variables from the DUSHIN program,[65] employing both curvilinear and rectilinear coordinate systems. The curvilinear coordinates are known to be better suited for distorted non-planar geometries (as in uracil), particularly as the Duschinsky matrix obtained with rectilinear coordinates is prone to display spurious couplings between low-frequency and high-frequency modes. We here present rate of IC computed using both.

For the purpose of calculating $k_{\rm IC}$, the time-dependent correlation function ($G^{\rm FC+HT}_{\rm IC}(t,t';m,m')$ as in Eq. (9)) is computed within a time interval of [-5ps:5ps] with 50000 time steps. Furthermore, to compute the IC rate constant, we have performed one-dimensional fast Fourier transformation (FFTW)[66] on the time-dependent correlation function. On the other hand, to compute $k_{\rm ISC}$, numerical integration is performed over the real part of the time-dependent correlation function $G_{\rm ISC}(t)$ as in Eq. (12) using a time interval of 10 ps and 50000 grid points with Simpson's one-third rule.[48] For both rate calculations, the upper limit of time integration is chosen in such a way that it considers all the frequencies. Additionally, to ensure that the time-dependent correlation functions converge within our chosen time interval, we have incorporated a Gaussian and Lorentzian damping function with damping parameters γ =2 cm^{-1} and γ =50 cm^{-1} to calculate the $G_{\rm ISC}(t)$ and $G^{\rm FC+HT}_{\rm IC}(t,t';m,m')$), respectively. The

physical meaning of the damping parameter has been discussed previously in Ref. 47.

The calculation of k_{IC} and k_{ISC} has been implemented as a stand-alone Fortran90 code.[67] An overview of the computational protocol is shown in Scheme 2.

4 Results and discussions

We validate our computational setup for evaluating the rate of IC using the azulene molecule, in Section 4.1 and we then apply the framework to understand the photophysical deactivation pathway of uracil, as detailed in Section 4.2.

4.1 Azulene

Azulene is an interesting small molecule known to violate Kasha´s rule by exhibiting $S_2 \rightarrow S_0$ fluorescence. This peculiarity is attributed to the large energy gap between the S_2 and S_1 states, and much smaller energy separation between S_1 and S_0.[68,69] This also corroborates with our finding of a large 1.89 eV energy gap between the S_2 and S_1 states. Therefore, azulene is commonly used it a suitable candidate to test the capacities of theoretical frameworks to capture correctly the radiative and non-radiative photophysics of other molecules.[57,68–73] We apply our framework to compute k_{IC} from $S_1 \rightarrow S_0$, having an energy gap of 1.41 eV and the norm of NAC being 3.04 bohr^{-1} We obtain an IC rate constant of 2.42×10^{11} s^{-1} and 2.54×10^{11} s^{-1} using curvilinear and rectilinear coordinates, respectively. This is in good agreement with the experimentally reported value of 5×10^{11} s^{-1},[68–70] and also with other theoretical findings.[71,73]

4.2 Uracil

UV-visible light excitation of uracil in gas phase leads primarily to population of the bright S_2 state and to the slightly higher-energy S_3 state. The lowest singlet-excited state (S_1) of uracil is a dark state with planar geometry. The optimized S_2 structure is non-planar at the chosen level of theory, even though some computational studies have characterized it to be a planar structure enabling them to exploit symmetry. We here consider the minimum, non-planar structure as obtained consistently at the TDDFT level. As we intend to study the deactivation pathways involved, we have calculated the energetic positioning of the singlet and triplet manifolds of uracil obtained at the MS-CASPT2(14e,10o)/cc-pVDZ level starting from the excited S_2 as shown in Fig. 3. Since we here focus on the deactivation process mainly starting from the S_2 state, we present the results obtained using this geometry.

We compute the rates associated with the possible spin-allowed IC pathways. The nature of the variation of the IC rate constants with the energy gap and the resulting rate constants are shown in Fig. 4 and Table 1. Although the S_3 state has a slight population transfer from the ground state via excitation, the resulting state decays immediately to the S_2 state with a rate constant of 2.12×10^{12} s^{-1} and the associated lifetime is 0.47 ps. As seen from the rates reported in Table 1, the choice of rectilinear or curvilinear coordinates have little influence over the computed rate constants. Semi-classical nuclear dynamical studies finds the same behavior with a lifetime of less than 0.2 ps.[24] Recently, using a laser-based thermal desorption technique in a time-resolved photo-ion yield measurement experiment, Ghafur *et al.*[30] have probed the ultrafast decay (0.2 ps) of the S_3 state, keeping the pump wavelength less than 250 nm.

Table 1 also reports the rate of IC from $S_2 \rightarrow S_1$, being the other prominent deactivation pathway within the singlet manifold, with rate constants of 3.78×10^{11} s^{-1} and the corresponding lifetime is 2.64 ps. Most experimental findings[6,19,21,30] have reported bi-exponential decay mechanisms with a lifetime of 0.05 – 0.25 and 1.1 – 3.2 ps. In contrast, Kang *et al.*[1] found a monoexponential decay mechanism with lifetime of 2.4 ps. On the other side, semi-classical dynamics have obtained a different decay behavior, sensitive to the level of theory, with an average time scale ranging from 0.5 – 0.75 ps.[12,13,15,16,18,23]. This time-scale has been attributed to transitions occurring either through the direct decay of the excited-state populations from the $S_2 \rightarrow S_0$[16,18] or from the $S_1 \rightarrow S_0$.[12,13,15]. However, Fingerhut *et al.*[23] ascribe it to a $S_2 \rightarrow S_1$ transition. In this context, it should also be highlighted that, although several experiments[3,7,19,21,30] and semi-classical dynamics[15,24,31,32] found decay time ranging from 0.05 – 0.25 and 0.01 – 0.07 ps, respectively, Hudock *et al.*[11] have argued this ultrafast femtosecond timescale to be the vibrational relaxation to the minima of the S_2 electronic state rather than population transfer to the lowest energy S_1 state. Their full multiple spawning study at the SA-CASSCF(8,6) level suggests the time scale of $S_2 \rightarrow S_1$ IC as 0.5 ps. Nevertheless, the decay time for the $S_2 \rightarrow S_1$ pathway as obtained with our code is approximately 5 times higher compared to the experimental result[3]. Earlier, it has been found that the inclusion of anharmonicity in the rate expression has increased the value of the IC rate constant[72] of azulene up to 30% or more. We believe that the inclusion of the anharmonicity in the present code in the future will definitely resolve the existing small discrepancy between the experimental decay time for the $S_2 \rightarrow S_1$ pathways and that of ours obtained with a FGR-based rate constant. It is important to mention here that we do not present the rate constant of IC between $S_1 \rightarrow S_0$ due to the large energy gap between the states, making it unfit for our Fermi´s Golden rule-based method. The rate of IC between the lowest two triplet states are also reported in Table 1, with k_{IC} of the order of 10^{10} s^{-1}. Even though the rate constant is high enough for this decay channel, the significance of this pathway however depends on the effectiveness of ISC from the singlet to the triplet manifold necessary for considerable population transfer to the T_2 state.

Eqn.(3) and (6) mathematically shows the factors governing the rate of IC on additional terms, such as the energy gap (ΔE), Dushchinsky rotation matrix (**J**), displacement vector (**D**) and frequencies (ω_S) of the involved electronic states, and most importantly the non-adiabatic coupling term between the electronic states. The mode-specific NAC vector contributions between the significant IC channels, $S_3 \rightarrow S_2$ and $S_2 \rightarrow S_1$ are depicted in Figs. 5 and 6, respectively at the MS-CASPT2 and CASSCF levels. We observe that the dominating contributing normal modes remain unchanged upon a change of the level of theory. It is also ev-

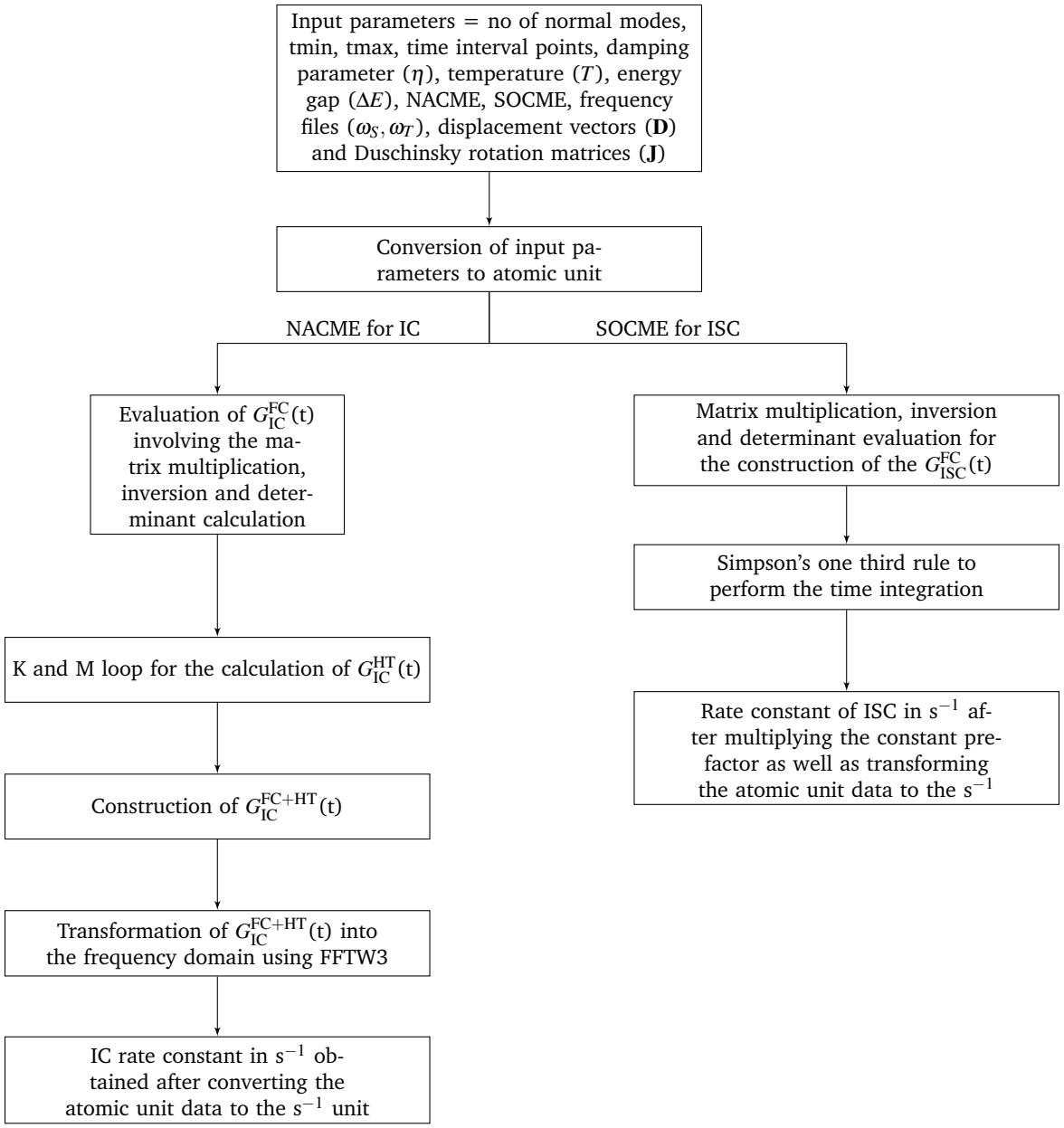

Fig. 2 Flow chart for the implemented protocols for computing the rate of IC[?] and ISC.

Table 1 Internal conversion rate constants calculated using the energy gap and NACME obtained at the S_2 geometry using the MS-CASPT2 level of theory with (14e,10o) active space. Here a and b denotes the rate constant (k_{IC}) and the corresponding lifetime (τ) evaluated involving the **J** and **D** computed in curvilinear and rectilinear coordinates, respectively.

Transition	ΔE (eV)	norm (Bohr^{-1})	k_{IC}^{a} (s^{-1})	τ^{a} (ps)	k_{IC}^{b} (s^{-1})	τ^{b} (ps)
$S_3 \rightarrow S_2$	0.52	4.86	2.12×10^{12}	0.47	1.07×10^{12}	0.93
$S_2 \rightarrow S_1$	0.21	4.12	3.78×10^{11}	2.64	2.47×10^{11}	4.04
$T_2 \rightarrow T_1$	0.72	0.77	4.65×10^{10}	21.50	3.77×10^{10}	26.52

ident from Figs. 5 and 6, that a few vibrational modes contribute more significantly towards IC than others. The number of normal modes having a major contribution towards the rate determination is larger for $S_3 \rightarrow S_2$ transitions compared to the $S_2 \rightarrow S_1$ transition, indicating a larger k_{IC} in the former route. In particular the NAC vector elements at frequencies of 2243 cm^{-1} in $S_2 \rightarrow S_1$ have considerably large contributions towards the IC rate constant than other modes. However, apart from this mode (mode no. 26), three other modes with frequencies 1314, 1505 and 1617 cm^{-1} corresponding to mode numbers 20, 24 and 25, respectively, also have notable contributions to the rate of IC.

We further compute the PESs associated with these vibrational modes in the three singlet excited states, as shown in Fig 7 at the MS-CASPT2 level of theory. The PESs of these vibrational

Table 2 Intersystem crossing rate constants computed using the energy gap and SOCME taken from the MS-CASPT2 and NEVPT2 method respectively with active space (14e,10o) computed at the S_2 geometry. The rate constants and the associated lifetimes calculated using **J** and **D** in curvilinear and rectilinear coordinates, are denoted by a and b respectively.

Transition	ΔE (eV)	SOC (cm^{-1})	k^a_{ISC} (s^{-1})	τ^a (ps)	k^b_{ISC} (s^{-1})	τ^b (ps)
$S_3 \rightarrow T_3$	0.34	56.18	1.19×10^{11}	8.40	1.11×10^{11}	9.00
$S_2 \rightarrow T_2$	0.30	19.44	1.04×10^{10}	96.15	4.88×10^{10}	20.49
$S_2 \rightarrow T_1$	1.02	15.28	8.97×10^{9}	111.48	7.22×10^{9}	138.50
$S_1 \rightarrow T_2$	0.09	9.46	6.57×10^{9}	152.20	6.57×10^{9}	152.20
$S_1 \rightarrow T_1$	0.81	53.10	1.37×10^{11}	7.29	1.11×10^{11}	9.00

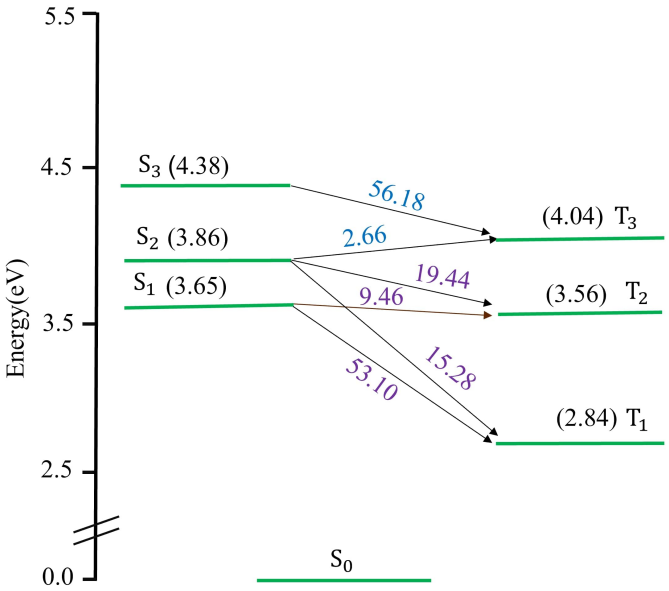

Fig. 3 Energy level of the excited states with respect to the ground state computed at the MS-CASPT2/(14e,10o) method using the S_2 geometry. The SOCMEs given over the arrow in cm^{-1} are obtained using NEVPT2 method.

modes at the CASSCF level are also supplied in the ESI. Here, we observe that the energy gap between the PESs of the uncoupled modes is very small which indeed would facilitate the ultrafast IC, even without accessible conical intersections as proposed by Mukherjee and Barbatti.[36]

Mode number 20 and 24 are N_2-H_{10} in-plane bending and N_2-C_3 as well as N_2-C_6 stretching with ethylenic C_1-H_8 bending in-plane character, respectively. Whereas, the 25th normal mode shows a complex motion associated with symmetric C_4-O_{12} and C_3-O_9, and ethylenic C_1-C_5 stretching with strong in-plane N_6-H_7 bending. The 26th mode involves the motion of antisymmetric C-O stretching with N_2-H_{10}, N_6-H_7 and slight ethylenic C_1-C_5 bending motion. It is evident from Fig 6 that mode 26 has a larger NACME than other modes between the S_2 and S_1 states, leading to a larger contribution to the net IC rate constants. The mode-specific k_{IC} value of mode 26 of $S_2 \rightarrow S_1$ is 2.11 $\times 10^{11}$ s^{-1}, whereas the total rate constant obtained by adding the k_{IC} of the individual normal modes 20, 24 and 25 is 6.91 $\times 10^{10}$ s^{-1}. The larger NACME in mode number 26 arises because of the close proximity of the S_2 and S_1 PESs, as evident from Fig 7. The displacement vectors associated with these vibrational normal modes are provided in the ESI.

In the present context, it is also to be noted that none of the normal modes alone can induce conical intersection (CI) between S_2 and S_1 in the harmonic region of the PESs and the optimization of the CI geometry at the MS-CASPT2/(14e,10o) level suggests that the C_3-O_9, C_3-N_6 and ethylenic C_1-C_5 bonds are stretched compared to the lengths of these bonds at the equilibrium S_2 geometry. The relative changes occurring in the CI geometry indicates that the commencement of CI is possible when mode 25 and 26 get coupled and the question remains unresolved how the coupling of such high-frequency normal modes is possible at room temperature, as canonical probability contributions of these modes are quite small. Nevertheless, to get a flavor of CI, starting from the CI geometry, we have generated a number of geometries using linear interpolation of internal coordinates (LIIC)[32,74] and have performed single-point energy calculations at the same level used to optimize the CI geometry. The PESs are provided in the ESI and probe the point of conical intersection. The present work actually demonstrates that internal conversion between S_2 and S_1 may occur partially via small-gap potential energy surfaces in selective normal modes, and partially through conical intersection.

We have until now restricted the discussion to the singlet manifold. In order to include the triplet states within the de-activation pathway, one has to consider the ISC process, leading to population gain within the triplet manifold. For this purpose, we have computed the rate of ISC among all the possible channels lower in energy than the S_3 state, that is, $S_3 \rightarrow T_3$, $S_2 \rightarrow T_2$, $S_2 \rightarrow T_1$, $S_1 \rightarrow T_2$ and $S_1 \rightarrow T_1$. The rate of ISC for each of the individual pathways are tabulated in Table 2, together with the energy gap and SOC between the singlet and triplet states.

The energy gap (ΔE) and the spin-orbit coupling (SOC) interaction[75–78] between the different spin states are the two fundamental parameters for predicting the feasibility of ISC. From Eq. (13) it is clear that stronger SOC and smaller energy gap between the different spin states promotes ISC, these parameters for uracil are presented in Fig. 3. It is worth mentioning here that Duschinsky rotation parameters (**J** and **D**) also play a vital role in determining the probability of ISC.[48,79] The qualitative discussion related to the magnitude of the spin-orbit coupling matrix element (SOCME) between the singlet and triplet levels are also given in ESI.

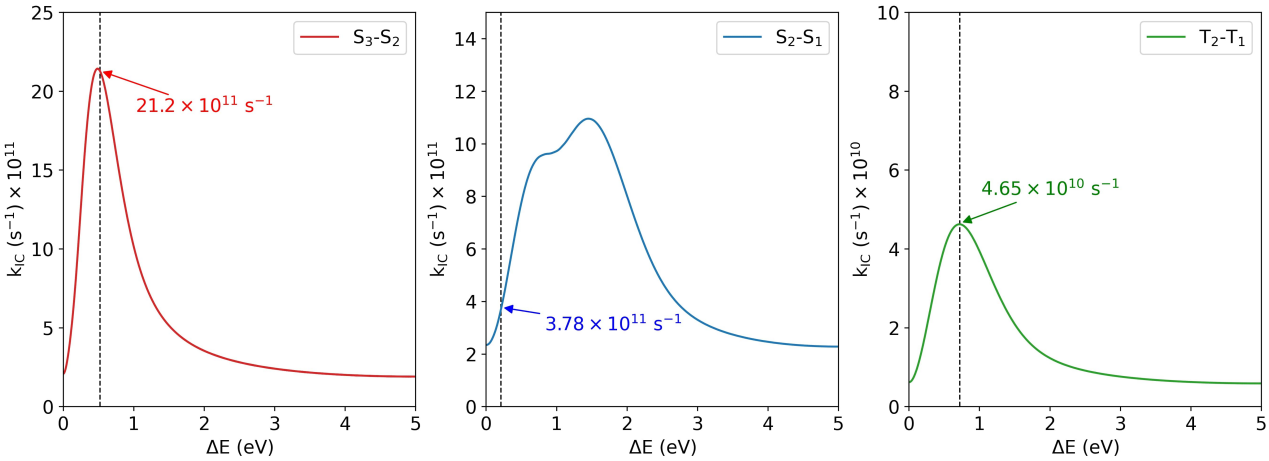

Fig. 4 Variation of k_{IC} with the energy gap at the MS-CASPT2/(14e,10o) method, where for the computation of rate constant, the J and D have been extracted using curvilinear coordinate.

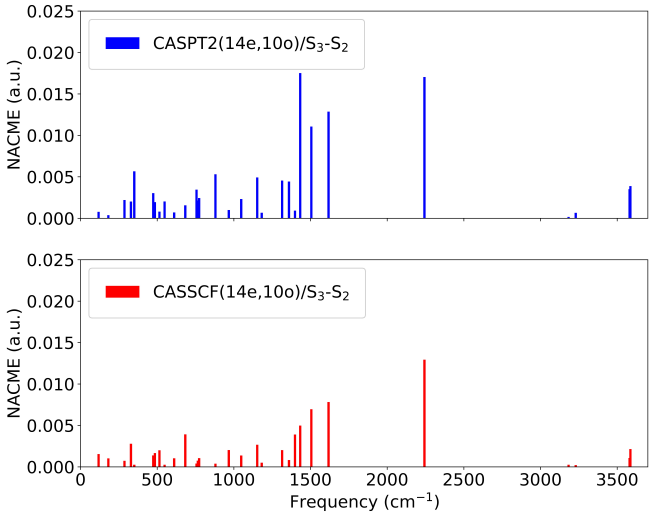

Fig. 5 Mode specific NACMEs between the S_3 and S_2 states..

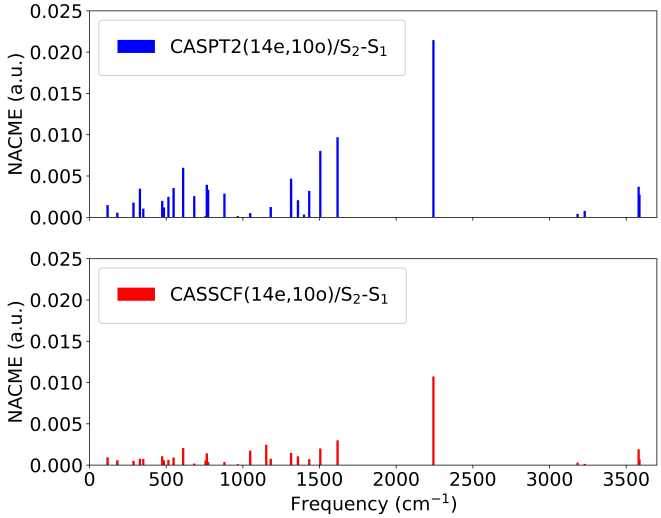

Fig. 6 Mode specific NACMEs between the S_2 and S_1 states.

Therefore, our calculated rates of IC and ISC reveal that there exist multiple competing deactivation pathways in uracil with comparable rate constants. This is unsurprising, given the ambiguity associated with the excited-state decay pathways reported in the literature.[1,3,6,11–13,15,16,18,21–24] Deactivation from the S_3 state is primarily via IC to S_2 rather than ISC to T_3 state. Furthermore, due to the lower intensity of the $S_0 \rightarrow S_3$ initial photoexcitation, the T_3 state is not sufficiently populated to open a new and significant deactivation IC channel within the triplet manifold originating from $T_3 \rightarrow T_2$. The decay pathways originating from the bright S_2 state is therefore the primary target. The calculated k_{ISC} of 1.04×10^{10} and 8.97×10^{9} s^{-1} for $S_2 \rightarrow T_2$ and $S_2 \rightarrow T_1$, respectively, to be compared to k_{IC} of 3.78×10^{11} s^{-1} between the $S_2 \rightarrow S_1$, highlights that IC most efficiently depopulates the S_2 state. Even though there is no experimentally measured ISC rate constant for these pathways, our results are in good agreement with those reported by Etinski *et al.*[80] obtained using the time-independent method.[81]. Notice here, that the rates obtained using curvilinear and rectilinear coordinate systems are comparable, as shown in Tables 1 and 2.

Investigating finally the decay channels available from the S_1 state, $S_1 \rightarrow T_1$ is the major pathway due to the larger SOC between them of 53.10 cm^{-1}, compared to $S_1 \rightarrow T_2$ (9.46 cm^{-1}). The corresponding rate constants between $S_1 \rightarrow T_1$ and $S_1 \rightarrow T_2$ are 1.37×10^{11} and 6.57×10^{9} s^{-1}, respectively. ISC from the S_1 state populates the triplet manifold, and in particular the T_1 state. Indeed, our computed lifetime of 7.29 ps associated with the S_1-T_1 ISC process is in good agreement with several experimental[1,3,6,9,19,21,30] and theoretical investigations[16,24,27]. There could also occur a competitive and simultaneous deactivation to

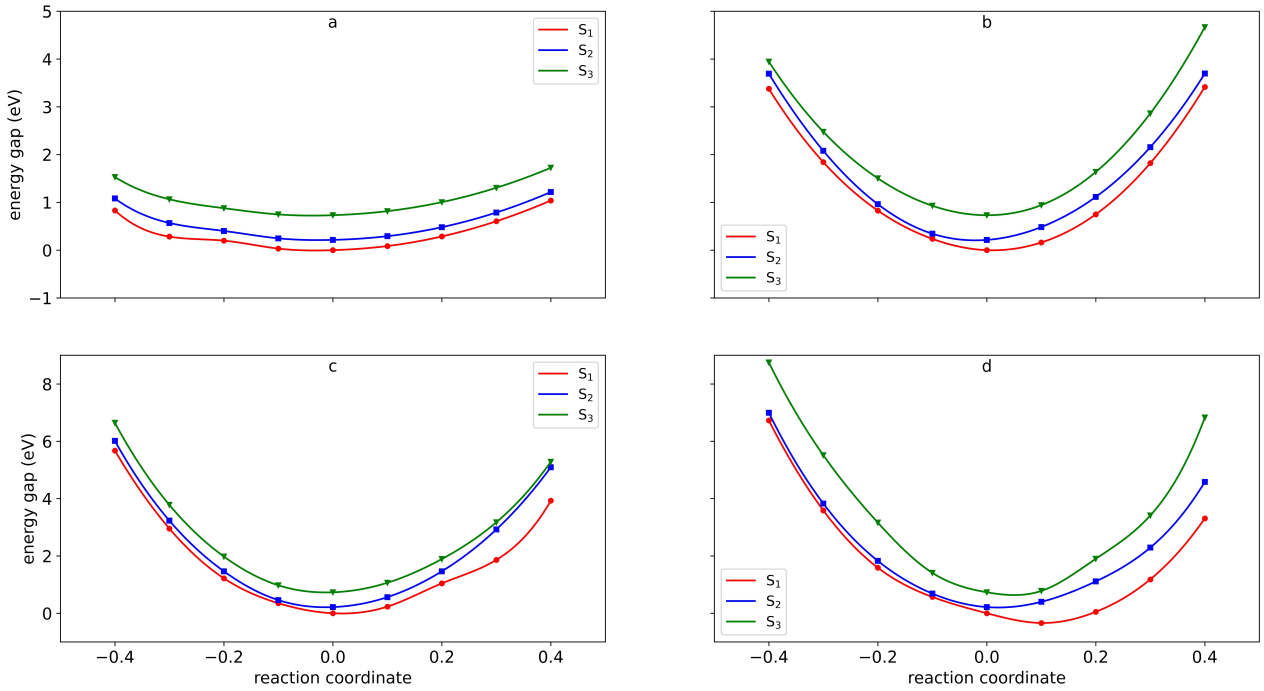

Fig. 7 Potential energy surfaces of normal modes obtained using MS- CASPT2/(14e,10o) method. Here the reaction coordinate indicate the manual displacement of the normal mode coordinate along the direction of the displacement vector of the respective normal mode. a, b, c and d denotes the potential energy surface for normal modes 20, 24, 25 and 26 with frequencies 1314, 1505, 1617 and 2243 cm^{-1}, respectively.

the S_0 state via radiative and/or non-radiative mechanisms.

From the above findings, we propose that the de-excitation mechanism of uracil follows the $S_2 \rightarrow S_1 \rightarrow T_1$ pathway, which is in good agreement with the results reported in Refs. 9,80. Another previously reported deactivation pathway is $S_2 \rightarrow S_1 \rightarrow T_2 \rightarrow T_1$, resulting in the suppression of the nonradiative $S_1 \rightarrow S_0$ IC, as well as direct transfer of the excitations from the $S_1 \rightarrow T_1$.[24]

5 Conclusions

In summary, we have presented a general methodology based on time-dependent correlation functions to calculate the rate of non-radiative deactivation processes, namely IC and ISC. The two processes are treated on an equal footing, with NAC and SOC being the main driving force behind IC and ISC, respectively. The energy gap is a common factor in determining the rate constants for the two. Our open-source implementation is highly flexible as it can use input parameters (energy gap, SOCME, NACME, frequency, Duschinsky rotation matrix and displacement vector parameters) obtained at any meaningful quantum-chemical theory level to calculate the rate constants. The computational scheme is validated by computing the rate of IC for $S_1 \rightarrow S_0$ transition in azulene, giving excellent agreement with experiment.

Further, to gauge the limits of our method, we study the highly complex photophysics of uracil. Firstly, we checked the applicability of the Fermi´s Golden rule-based approach for studying the photodynamics of uracil by generating the electronic state mode-specific PESs. We observed that quite a few of the contributing vibrational modes have almost parallel PES with small energy separation. Under such circumstances, even though the probability of transition is less due to small NACME, there exists many more instances for transition, leading to ultrafast IC. Our rate calculations show that the decay pathway is indeed quite complex, with no single pathway outperforming others. This was to be expected given the conflicting results in the literature regarding the exact mechanism of decay. We have found that the initially excited bright S_2 state promptly decays to the S_1 state. The most challenging pathway has been the loss of population from the S_1 state, which has two simultaneous decay pathways, (1) $S_1 \rightarrow S_0$ internal conversion, the rates of which we do not compute with our approach due to the high energy gap between the S_1 and S_0 states (2) a direct $S_1 \rightarrow T_1$ ISC with a lifetime of 7.29 ps. We also trace the deactivation pathway for the slightly populated S_3 state, which rapidly undergoes IC to the S_2 state. We conclude that after excitation, uracil follows $S_3 \rightarrow S_2 \rightarrow S_1 \rightarrow T_1$ pathway and subsequent decay to the S_0 state through radiative or non-radiative mechanisms. Due to a smaller population in the S_3 state, the chance of decay by spin-forbidden ISC to the triplet manifolds is extremely low. The suitability of our FGR based method for simulating ultrafast dynamics can be further validated by performing non-perturbative ab-initio quantum dynamics simulations of small- to medium-sized molecule including Duschinsky mixing ef-

fects.[33]

Author Contributions

S.C. and K.R. conceptualized the project. S.C. supervised the project. The implementation, calculation and analysis were performed by P.K. and T.M. All authors contributed to the writing of the manuscript. P.K. and T.M. contributed equally to this work.

Conflicts of interest

There are no conflicts to declare.

Acknowledgements

P. K. thanks the Council of Scientific and Industrial Research (CSIR) for granting him the Senior Research Fellowship. K.R. has received support from the Research Council of Norway through a Centre of Excellence Grant (grant number 262695). T.M. and K.R. acknowledges the support from the Norwegian research council grant number 315822. This work has received support from the Norwegian Supercomputer Program NOTUR (Grant No. NN4654K). The support and resources provided by 'PARAM Shakti Facility' under the National Supercomputing Mission, Government of India at the Indian Institute of Technology, Kharagpur, are gratefully acknowledged by S.C.

Notes and references

1 H. Kang, K. T. Lee, B. Jung, Y. J. Ko and S. K. Kim, *J. Am. Chem. Soc.*, 2002, **124**, 12958–12959.

2 H. Kang, B. Jung and S. K. Kim, *J. Chem. Phys.*, 2003, **118**, 6717–6719.

3 S. Ullrich, T. Schultz, M. Z. Zgierski and A. Stolow, *Phys. Chem. Chem. Phys.*, 2004, **6**, 2796–2801.

4 R. Improta and V. Barone, *J. Am. Chem. Soc.*, 2004, **126**, 14320–14321.

5 E. Samoylova, H. Lippert, S. Ullrich, I. V. Hertel, W. Radloff and T. Schultz, *J. Am. Chem. Soc.*, 2005, **127**, 1782–1786.

6 C. Canuel, M. Mons, F. Piuzzi, B. Tardivel, I. Dimicoli and M. Elhanine, *J. Chem. Phys.*, 2005, **122**, 074316.

7 T. Gustavsson, A. Bányász, E. Lazzarotto, D. Markovitsi, G. Scalmani, M. J. Frisch, V. Barone and R. Improta, *J. Am. Chem. Soc.*, 2006, **128**, 607–619.

8 F. Santoro, V. Barone, T. Gustavsson and R. Improta, *J. Am. Chem. Soc.*, 2006, **128**, 16312–16322.

9 P. M. Hare, C. E. Crespo-Hernández and B. Kohler, *Proc. Natl. Acad. Sci. U.S.A.*, 2007, **104**, 435–440.

10 E. Samoylova, T. Schultz, I. Hertel and W. Radloff, *Chem. Phys.*, 2008, **347**, 376–382.

11 H. R. Hudock, B. G. Levine, A. L. Thompson, H. Satzger, D. Townsend, N. Gador, S. Ullrich, A. Stolow and T. J. Martínez, *J. Phys. Chem. A*, 2007, **111**, 8500–8508.

12 N. L. Doltsinis, P. R. L. Markwick, H. Nieber and H. Langer, in *Ultrafast Radiationless Decay in Nucleic Acids: Insights From Nonadiabatic Ab Initio Molecular Dynamics*, ed. M. K. Shukla and J. Leszczynski, Springer Netherlands, Dordrecht, 2008, pp. 265–299.

13 H. Nieber and N. L. Doltsinis, *Chem. Phys.*, 2008, **347**, 405–412.

14 G. Zechmann and M. Barbatti, *J. Phys. Chem. A*, 2008, **112**, 8273–8279.

15 Z. Lan, E. Fabiano and W. Thiel, *J. Phys. Chem. B*, 2009, **113**, 3548–3555.

16 M. Barbatti, A. J. A. Aquino, J. J. Szymczak, D. Nachtigallová, P. Hobza and H. Lischka, *Proc. Natl. Acad. Sci. U.S.A.*, 2010, **107**, 21453–21458.

17 R. Improta, A. Lami, V. Barone and F. Santoro, *Int. J. Quantum Chem.*, 2010, **110**, 624–636.

18 D. Nachtigallová, A. J. A. Aquino, J. J. Szymczak, M. Barbatti, P. Hobza and H. Lischka, *J. Phys. Chem. A*, 2011, **115**, 5247–5255.

19 M. Kotur, T. C. Weinacht, C. Zhou and S. Matsika, *IEEE J. Sel. Top. Quantum Electron.*, 2012, **18**, 187–194.

20 F. J. Avila Ferrer and F. Santoro, *Phys. Chem. Chem. Phys.*, 2012, **14**, 13549–13563.

21 S. Matsika, M. Spanner, M. Kotur and T. C. Weinacht, *J. Phys. Chem. A*, 2013, **117**, 12796–12801.

22 B. P. Fingerhut, K. E. Dorfman and S. Mukamel, *J. Phys. Chem. Lett.*, 2013, **4**, 1933–1942.

23 B. P. Fingerhut, K. E. Dorfman and S. Mukamel, *J. Chem. Theor. Comput.*, 2014, **10**, 1172–1188.

24 M. Richter, S. Mai, P. Marquetand and L. González, *Phys. Chem. Chem. Phys.*, 2014, **16**, 24423–24436.

25 M. Ligare, F. Siouri, O. Bludsky, D. Nachtigallová and M. S. de Vries, *Phys. Chem. Chem. Phys.*, 2015, **17**, 24336–24341.

26 M. M. Brister and C. E. Crespo-Hernández, *J. Phys. Chem. Lett.*, 2015, **6**, 4404–4409.

27 H. Yu, J. A. Sanchez-Rodriguez, M. Pollum, C. E. Crespo-Hernández, S. Mai, P. Marquetand, L. González and S. Ullrich, *Phys. Chem. Chem. Phys.*, 2016, **18**, 20168–20176.

28 R. Improta, F. Santoro and L. Blancafort, *Chem. Rev.*, 2016, **116**, 3540–3593.

29 T. J. A. Wolf, R. H. Myhre, J. P. Cryan, S. Coriani, R. J. Squibb, A. Battistoni, N. Berrah, C. Bostedt, P. Bucksbaum, G. Coslovich, R. Feifel, K. J. Gaffney, J. Grilj, T. J. Martinez, S. Miyabe, S. P. Moeller, M. Mucke, A. Natan, R. Obaid, T. Osipov, O. Plekan, S. Wang, H. Koch and M. Gühr, *Nat. Commun.*, 2017, **8**, 29.

30 O. Ghafur, S. W. Crane, M. Ryszka, J. Bockova, A. Rebelo, L. Saalbach, S. De Camillis, J. B. Greenwood, S. Eden and D. Townsend, *J. Chem. Phys.*, 2018, **149**, 034301.

31 P. Chakraborty, Y. Liu, S. McClung, T. Weinacht and S. Matsika, *J. Phys. Chem. Lett.*, 2021, **12**, 5099–5104.

32 P. Chakraborty, Y. Liu, T. Weinacht and S. Matsika, *Faraday Discuss.*, 2021, **228**, 266–285.

33 J. A. Green, M. Y. Jouybari, D. Aranda, R. Improta and F. Santoro, *Molecules*, 2021, **26**, 1–23.

34 D. A. Fedotov, A. C. Paul, P. Posocco, F. Santoro, M. Garavelli, H. Koch, S. Coriani and R. Improta, *J. Chem. Theor. Comput.*, 2021, **17**, 1638–1652.

35 C. A. Farfan and D. B. Turner, *J. Phys. Chem. A*, 2019, **123**, 7768–7776.

36 S. Mukherjee and M. Barbatti, *Results in Chemistry*, 2022, **4**, 100521.

37 F. Aleotti, D. Aranda, M. Yaghoubi Jouybari, M. Garavelli, A. Nenov and F. Santoro, *J. Chem. Phys.*, 2021, **154**, 104106.

38 S. Mukherjee and S. A. Varganov, *J. Chem. Phys.*, 2021, **155**, 174107.

39 R. Kubo, *Phys. Rev.*, 1952, **86**, 929–937.

40 R. Kubo and Y. Toyozawa, *Prog. Theor. Phys.*, 1954, **12**, 805–806.

41 R. Kubo and Y. Toyozawa, *Prog. Theor. Phys.*, 1955, **13**, 160–182.

42 Q. Peng, Y. Yi, Z. Shuai and J. Shao, *J. Chem. Phys.*, 2007, **126**, 114302.

43 Q. Peng, Y. Niu, Q. Shi, X. Gao and Z. Shuai, *J. Chem. Theory Comput.*, 2013, **9**, 1132–1143.

44 A. Baiardi, J. Bloino and V. Barone, *J. Chem. Theory Comput.*, 2013, **9**, 4097–4115.

45 Q. Peng, D. Fan, R. Duan, Y. Yi, Y. Niu, D. Wang and Z. Shuai, *J. Phys. Chem. C*, 2017, **121**, 13448–13456.

46 Y. Liu, D. Aranda and F. Santoro, *Phys. Chem. Chem. Phys.*, 2021, **23**, 16551–16563.

47 T. Moitra, M. M. Alam and S. Chakrabarti, *Phys. Chem. Chem. Phys.*, 2018, **20**, 23244–23251.

48 P. Karak and S. Chakrabarti, *Phys. Chem. Chem. Phys.*, 2020, **22**, 24399–24409.

49 P. Karak, K. Ruud and S. Chakrabarti, *J. Phys. Chem. Lett.*, 2021, **12**, 9768–9773.

50 P. Karak, K. Ruud and S. Chakrabarti, *J. Chem. Phys.*, 2022, **157**, 174101.

51 Y. Niu, Q. Peng, C. Deng, X. Gao and Z. Shuai, *J. Phys. Chem. A*, 2010, **114**, 7817–7831.

52 S. Banerjee, A. Baiardi, J. Bloino and V. Barone, *J. Chem. Theory Comput.*, 2016, **12**, 774.

53 R. Ianconescu and E. Pollak, *J. Phys. Chem. A*, 2004, **108**, 7778.

54 M. Etinski, J. Tatchen and C. Marian, *J. Chem. Phys.*, 2011, **134**, 154105.

55 M. J. Frisch, G. W. Trucks, H. B. Schlegel, G. E. Scuseria, M. A. Robb, J. R. Cheeseman, G. Scalmani, V. Barone, G. A. Petersson, H. Nakatsuji, X. Li, M. Caricato, A. V. Marenich, J. Bloino, B. G. Janesko, R. Gomperts, B. Mennucci, H. P. Hratchian, J. V. Ortiz, A. F. Izmaylov, J. L. Sonnenberg, D. Williams-Young, F. Ding, F. Lipparini, F. Egidi, J. Goings, B. Peng, A. Petrone, T. Henderson, D. Ranasinghe, V. G. Zakrzewski, J. Gao, N. Rega, G. Zheng, W. Liang, M. Hada, M. Ehara, K. Toyota, R. Fukuda, J. Hasegawa, M. Ishida, T. Nakajima, Y. Honda, O. Kitao, H. Nakai, T. Vreven, K. Throssell, J. A. Montgomery, Jr., J. E. Peralta, F. Ogliaro, M. J. Bearpark, J. J. Heyd, E. N. Brothers, K. N. Kudin, V. N. Staroverov, T. A. Keith, R. Kobayashi, J. Normand, K. Raghavachari, A. P. Rendell, J. C. Burant, S. S. Iyengar, J. Tomasi, M. Cossi, J. M. Millam, M. Klene, C. Adamo, R. Cammi, J. W. Ochterski, R. L. Martin, K. Morokuma, O. Farkas, J. B. Foresman and D. J. Fox, *Gaussian 16 Revision C.01*, 2016, Gaussian Inc. Wallingford CT.

56 J. Finley, P. Åke Malmqvist, B. O. Roos and L. Serrano-Andrés, *Chem. Phys. Lett.*, 1998, **288**, 299–306.

57 M. J. Bearpark, F. Bernardi, S. Clifford, M. Olivucci, M. A. Robb, B. R. Smith and T. Vreven, *J. Am. Chem. Soc.*, 1996, **118**, 169–175.

58 T. H. Dunning, *J. Chem. Phys.*, 1989, **90**, 1007–1023.

59 M. K. MacLeod and T. Shiozaki, *J. Chem. Phys.*, 2015, **142**, 051103.

60 B. Vlaisavljevich and T. Shiozaki, *J. Chem. Theor. Comput.*, 2016, **12**, 3781–3787.

61 J. W. Park and T. Shiozaki, *J. Chem. Theor. Comput.*, 2017, **13**, 3676–3683.

62 J. W. Park and T. Shiozaki, *J. Chem. Theor. Comput.*, 2017, **13**, 2561–2570.

63 F. Neese, *Wiley Interdiscip. Rev. Comput. Mol. Sci.*, 2012, **2**, 73–78.

64 F. Neese, *Wiley Interdiscip. Rev. Comput. Mol. Sci.*, 2018, **8**, e1327.

65 J. R. Reimers, *J. Chem. Phys.*, 2001, **115**, 9103–9109.

66 M. Frigo and S. Johnson, *Proc. IEEE*, 2005, **93**, 216–231.

67 P. Karak and S. Chakrabarti, *swapanchem/IC_RATE_CONSTANT_MPI: IC_RATE_CONSTANT_MPI*, 2023, `https://doi.org/10.5281/zenodo.7597456`.

68 G. D. Gillispie and E. C. Lim, *J. Chem. Phys.*, 1978, **68**, 4578–4586.

69 K. Gustav and M. Storch, *Int. J. Quantum Chem.*, 1990, **38**, 1–10.

70 E. Ippen, C. Shank and R. Woerner, *Chem. Phys. Lett.*, 1977, **46**, 20–23.

71 R. Islampour and M. Miralinaghi, *J. Phys. Chem. A*, 2007, **111**, 9454–9462.

72 Y. Wang, J. Ren and Z. Shuai, *J. Chem. Phys.*, 2021, **154**, 214109.

73 K. Miyazaki and N. Ananth, *J. Chem. Phys.*, 2022, **156**, 044111.

74 Y. Mercier, F. Santoro, M. Reguero and R. Improta, *J. Phys. Chem. B*, 2008, **112**, 10769–10772.

75 T. Moitra, P. Karak, S. Chakraborty, K. Ruud and S. Chakrabarti, *Phys. Chem. Chem. Phys.*, 2021, **23**, 59–81.

76 H. Ågren, O. Vahtras and B. Minaev, *Adv. Quantum Chem.*, 1996, **27**, 71–164.

77 T. J. Penfold, E. Gindensperger, C. Daniel and C. M. Marian, *Chem. Rev.*, 2018, **118**, 6975–7025.

78 C. M. Marian, *WIREs Comput. Mol. Sci.*, 2012, **2**, 187–203.

79 L. Paul, T. Moitra, K. Ruud and S. Chakrabarti, *J. Phys. Chem. Lett.*, 2019, **10**, 369–374.

80 M. Etinski, T. Fleig and C. M. Marian, *J. Phys. Chem. A*, 2009, **113**, 11809–11816.

81 J. Tatchen, N. Gilka and C. M. Marian, *Phys. Chem. Chem. Phys.*, 2007, **9**, 5209–5221.